Full waveform inversion of DAS field data from the 2018 CaMI VSP survey

Matt Eaid, Scott Keating, and Kris Innanen

ABSTRACT

Carbon capture and storage has become a key research area for diverting carbon dioxide gas away from the atmosphere by storing it in deep subsurface reservoirs. Seismic data are a key technology for monitoring the injected carbon dioxide to ensure that it remains in the target formation and does not migrate into regions where it may pose a risk. Distributed acoustic sensing permits permanent installation of receivers in borehole geometries, allowing for highly repeatable sampling of transmission wavefield modes which is crucial for seismic monitoring surveys. To fully leverage the data supplied by DAS fibers, the inverse methods developed by Eaid et al. (2020) must transfer to DAS data acquired in the field both in isolation and in combination with accelerometer data. In 2018, the Consortium for Research in Elastic Wave Exploration Seismology acquired a 3D walkaway-walkaround VSP survey into both three-component accelerometers and DAS fiber. In this report the DAS fiber data are inverted using isotropic-elastic full waveform inversion. A method for the source wavefield estimation and a log-derived model parameterization are found to be crucial for convergence of the inverted models in FWI. Inverting the DAS data independently provides robust parameter estimates of the subsurface P-wave velocity, S-wave velocity, and density structure with a good fit between modeled and field data. However, inverting both datasets together using a newly formulated objective function that provides a means of controlling the relative emphasis on DAS and accelerometer data is shown to have a stabilizing effect on the inverted models when compared to using either dataset alone.

INTRODUCTION

Climate change is one of the most significant challenges that Earth faces. The consensus of the scientific community that the main driver for climate change is the anthropogenic release of greenhouse gases (Rodhe, 1990; Oreskes, 2004; Cook et al., 2013; Kweku et al., 2017). As these gases are generated, they rise into the atmosphere where they linger, trap heat from the sun, destabilize the global climate. Left unchecked, these greenhouse gases are expected to trap increasingly more energy from the sun, which is projected to lead to more frequency and severe weather patterns across Earth. Carbon dioxide (CO_2), produced as a by-product of combustion, is a particularly prolific green house gas.

Carbon capture and storage (CCS) is an area of research aimed at reducing the effect of atmospheric CO_2 by diverting it away from the atmosphere during industrial processes using a capture technology. The captured CO_2 is then transported (typically by pipeline) to a field site where it is injected into reservoirs for long term storage. A major concern for CCS is the possibility for CO_2 to escape from the desired reservoir, accumulate in near surface reservoirs, and then escape into the atmosphere. This would negate the benefits of CCS, and has the potential for a sudden and catastrophic release of carbon dioxide that could create significant health problems for people in the immediate vicinity.

The development of technologies for monitoring injected CO_2 is a key goal of many CCS projects. Ideally, these technologies would allow for the tracking of the plume over time, ensuring it remains in the target reservoir, and allowing for the detection of leaks before they become a significant problem. Seismic monitoring is a key technology for facilitating the safe storage of CO_2 in deep subsurface reservoirs. Using seismic monitoring for CCS projects involves collection of a baseline seismic survey prior to fluid injection, and recurring monitor surveys after various stages of fluid injection. If the same seismic acquisition is used for the baseline and monitor surveys, and minimal seasonal variation occurs in the near surface, then changes in the seismic data between surveys will be related to the injected CO_2. The variation in the seismic data can be used to track its location, extent, and its properties, allowing seismic monitoring to provide a high resolution image of the injected fluid.

The Containment and Monitoring Institute (CaMI) under Carbon Management Canada (CMC) focuses on the development of technologies for monitoring injected carbon dioxide at its Field Research Station in Brooks, Alberta. The goal of the FRS is the development of methods for monitoring the growth of a CO_2 plume maintained in the water filled Basal Belly River sandstone unit of Upper Cretaceous age at a depth of 300 meters (Isaac and Lawton, 2016). To facilitate this goal, a vertical seismic profile (VSP) baseline survey was acquired in 2018 using accelerometers and collocated distributed acoustic sensing (DAS) fiber in a monitoring well located approximately 20 meters southwest of the injector well. In this report, the accelerometer data, and DAS data which were processed in a companion report (Eaid et al., 2021) are used in full waveform inversion to support the estimation of subsurface parameter distributions for the baseline survey.

CONTAINMENT AN MONITORING INSTITUTE 2018 VSP SURVEY

The chief goal of the Containment and Monitoring Institutes Field Research Station (located near Brooks, Alberta see Figure 1) is the development of technologies and processes for monitoring CO_2 sequestered in the late Cretaceous Basal Belly River Sandstone at 300 meters depth (Lawton et al., 2018; Macquet et al., 2019; Spackman, 2019). Amongst the proposed technologies for realizing this goal, seismic monitoring is projected to be a key tool for imaging of the CO_2 plume. To support seismic monitoring many acquisition tools have been deployed at the field research station (FRS). The FRS houses three wells, including the well being used for CO_2 injection, and two observation wells. Observation well 2, colloquially referred two as the geophysics well permanently houses a straight DAS fiber, and a helically wound fiber with a lead angle of $30°$. In a companion report (Eaid et al., 2021), the field data from the accelerometers and straight DAS fiber were processed in preparation for FWI. Keating et al. (2021b) report on full waveform inversion of the accelerometer data, while the focus of this report is inversions of the DAS fiber data, both in isolation and in combination with the accelerometer data. Figure 2 plots the source geometry for the VSP survey with the source line of interest highlighted in blue. Figure 3 plots the processed DAS data from Eaid et al. (2021) for every 6^{th} shot point on source line 1.

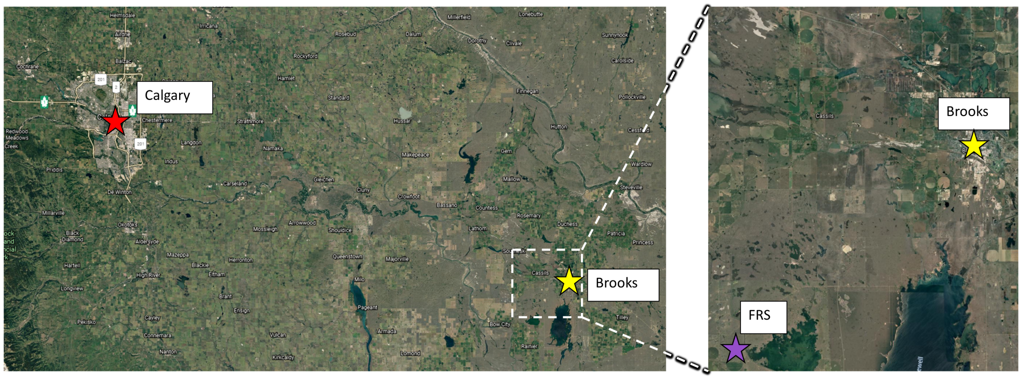

FIG. 1. Location of the CaMI FRS in Newell Country, in relation to Calgary, Alberta, and Brooks, Alberta.

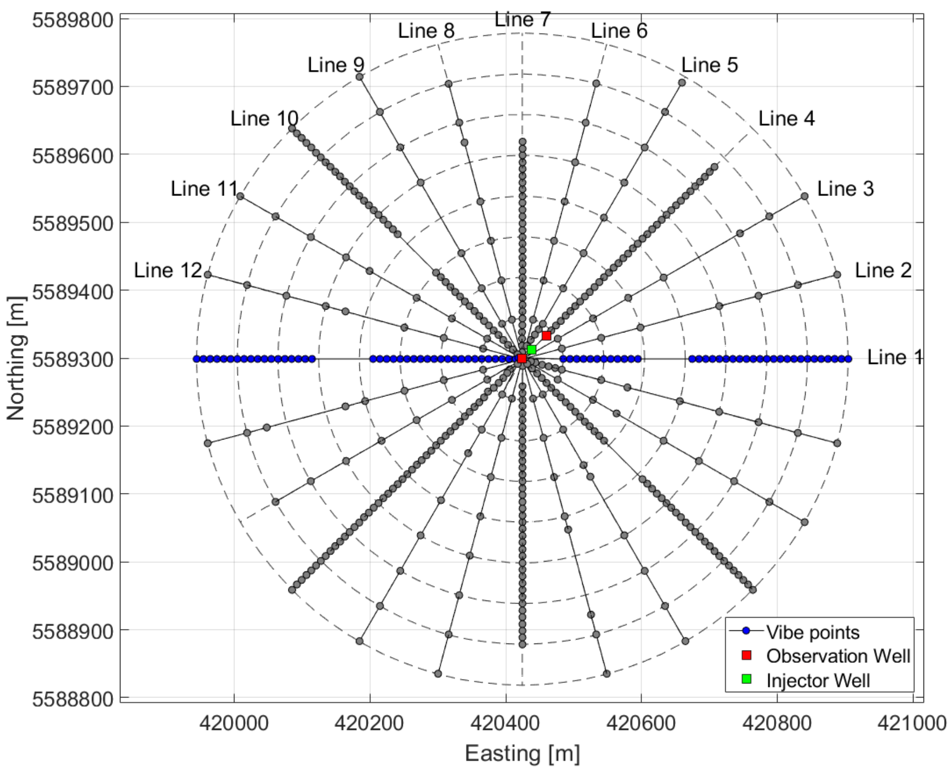

FIG. 2. Shot geometry of the CaMI-FRS 2018 3D walkaway-walkaround VSP. The blue circles represent shot point locations on source line 1, the red squares the locations of the two observation wells (Observation well 2 is at the center of the shot points), and the green square the location of the injector well. The dotted lines are 60 meter concentric circles centered on observation well 2.

FULL WAVEFORM INVERSION OF DAS DATA

The DAS field data in Figure 3 will be used in a frequency-domain full waveform inversion (FWI) method to invert for the subsurface distribution of isotropic-elastic parameters. Before presenting results of the inversion we will briefly review the requirements for including DAS data in FWI, and some of the considerations that were required to help the

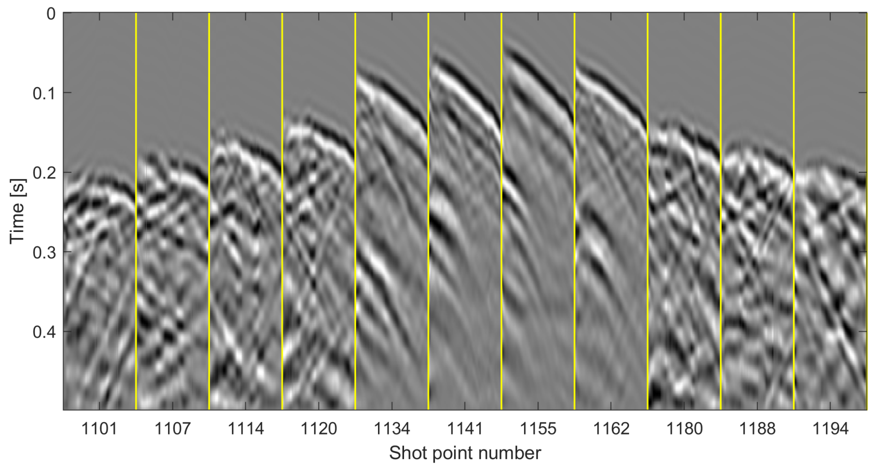

FIG. 3. Processed DAS data for every 6^{th} shot point point on source line 1.

FWI converge on geologically reasonable models using the field data. A detailed discussion for including DAS data in FWI is summarized by Eaid et al. (2020).

FWI is often presented as a constrained optimization problem of the form (Métivier et al., 2013),

$$\mathcal{L}(\mathbf{m}, \mathbf{u}, \kappa) = \frac{1}{2}||\mathbf{R}\mathbf{u}(\mathbf{m}) - \mathbf{d}||_2^2 + \big\langle \mathbf{S}(\mathbf{m})\mathbf{u} - \mathbf{f}, \kappa \big\rangle, \tag{1}$$

where $\mathcal{L}$ is a Lagrangian, $\mathbf{m}$ are the model parameters, $\mathbf{u}$ are modeled wavefields, κ is the Lagrange multiplier, $\mathbf{R}$ is a receiver sampling matrix, $\mathbf{d}$ are observed data, $\mathbf{S}$ is the wave equation operator, and $\mathbf{f}$ is the forcing function. Minimizing equation (1) consists of finding the model parameters $\mathbf{m}$ that minimize the misfit between the observed data $\mathbf{d}$ and modeled data $\mathbf{Ru}$ subject to the condition that the wavefield $\mathbf{u}$ satisfies the wave equation $\mathbf{Su} - \mathbf{f} = 0$. Finding this model is achieved by finding the stationary points of the Lagrangian,

$$\frac{\partial \mathcal{L}}{\partial \mathbf{m}} = 0 \;\; ; \;\; \frac{\partial \mathcal{L}}{\partial \mathbf{u}} = 0 \;\; ; \;\; \frac{\partial \mathcal{L}}{\partial \kappa} = 0. \tag{2}$$

The last of these stationary points ($\partial\mathcal{L}/\partial\kappa$) is found by letting $\bar{\mathbf{u}}$ be the wavefield that satisfies the wave equation. The gradient is found by letting $\bar{\mathbf{u}}$ satisfy the wave equation and taking the derivative of equation (1) with respect to the model parameters,

$$\frac{\partial \mathcal{L}(\mathbf{m}, \bar{\mathbf{u}}, \kappa)}{\partial \mathbf{m}} = \nabla\phi_D = \frac{\partial \mathcal{L}(\mathbf{m}, \bar{\mathbf{u}}, \kappa)}{\partial \bar{\mathbf{u}}(\mathbf{m})}\frac{\partial \bar{\mathbf{u}}(\mathbf{m})}{\partial \mathbf{m}} + \left\langle \frac{\partial \mathbf{S}}{\partial \mathbf{m}}\bar{\mathbf{u}}(\mathbf{m}), \kappa \right\rangle = 0. \tag{3}$$

The partial derivative wavefields ($\partial\bar{\mathbf{u}}/\partial\mathbf{m}$) are too cumbersome to compute, and prevent direct solutions of equation (3). To avoid their computation, we assume that $\partial\mathcal{L}/\partial\bar{\mathbf{u}}$ is a stationary point, and then find the condition that enforces this assumption. The derivative of the Lagrangian with respect to the wavefield is,

$$\frac{\partial \mathcal{L}(\mathbf{m}, \bar{\mathbf{u}}, \bar{\kappa})}{\partial \bar{\mathbf{u}}(\mathbf{m})} = 2\mathbf{R}^{\mathrm{T}}\mathbf{R}\bar{\mathbf{u}}(\mathbf{m}) - 2\mathbf{R}^{\mathrm{T}}\mathbf{d} + 2\mathbf{S}^{\dagger}\bar{\kappa} = 0 \tag{4}$$

which has the solution,

$$\mathbf{S}^{\dagger}\bar{\kappa} = \mathbf{R}^{\mathrm{T}}(\mathbf{R}\bar{\mathbf{u}}(\mathbf{m}) - \mathbf{d}). \tag{5}$$

The gradient is therefore,

$$\frac{\partial \mathcal{L}(\mathbf{m}, \bar{\mathbf{u}}, \bar{\kappa})}{\partial \mathbf{m}} = \left\langle \frac{\partial \mathbf{S}}{\partial \mathbf{m}} \bar{\mathbf{u}}(\mathbf{m}), \bar{\kappa} \right\rangle \tag{6}$$

where $\bar{\kappa}$ is the adjoint wavefield satisfying equation (5).

Inclusion of DAS data in FWI

It is conventionally assumed in FWI that the observed data and modeled data, compared in the objective function, are provided by orthogonal point sensors such as geophones. Distributed acoustic sensing (DAS) employs optical fibers to provide measurements of seismically induced strain along the tangent of the fiber (Kuvshinov, 2015; Innanen and Eaid, 2017; Eaid et al., 2018). The inclusion of DAS data in FWI then requires an objective function that can compare observed and modeled strain sampled along the tangent of a fiber embedded in the subsurface. If we assume geophone type sensors in the derivation of the FWI gradient, then **R** ostensibly acts to sample the wavefield **u** in up to three orthogonal directions. However, **R** can be more loosely interpreted as a sampling matrix that converts the modeled wavefield into data that can be directly compared to the field data. This means that if we formulate **R** in such a way that it incorporates properties of DAS receivers, then equations (1)-(6) are also applicable to DAS data. This allows us to use any standard FWI algorithm by simply reformulating the wavefield sampling matrix **R**. Specifically, when incorporating DAS data, **R** is responsible for

1. Computing the strain field along the DAS fiber
2. Applying gauge length averaging
3. Computing the DAS datum (tangential strain) for each receiver location along the fiber

The specifics of modeling the DAS data for items 1-3 above can be found in Eaid et al. (2020).

CONSIDERATIONS FOR ELASTIC FULL WAVEFORM INVERSION OF FIELD DATA

Inversion of field seismic data, especially from land base acquisition is a difficult proposition. Uncertainty in the near surface structure, incomplete treatment of the wave physics, cross-talk, limitations on the acquisition geometry, and limited prior model information are all challenges that compound to make land based challenging. Due to this, most of the successful applications of multiparameter FWI have been reported on marine data. VSP acquisition can help mitigate some of these challenges, however, as will be shown, adaptations to the FWI algorithm will be required.

Log guided model parameterization

FWI of the field data in this report will be restircted to an isotropic-elastic formulation. Hall et al. (2018) concluded that if anisotropy exists at the FRS, it is very weak and unlikely to significantly influence the data. Attenuation, especially in the near surface, is likely to play a larger role in wave propagation, however it adds a significant layer of complexity both in the wave physics, and parameter estimation in FWI. The focus of this study is the inclusion of DAS data in FWI so I restrict my analysis to an isotopic-elastic medium. Using the elastic stress-strain relation, the finite difference equations required for generation of the modeled data are,

$$\rho\omega^2\mathbf{u}+c_{11}\nabla(\nabla\cdot\mathbf{u})-c_{44}\nabla\times(\nabla\times\mathbf{u})+\nabla(c_{11}-2c_{44})(\nabla\cdot\mathbf{u})+\nabla c_{44}(\nabla\mathbf{u}+\nabla\mathbf{u}^{\mathrm{T}})+\mathbf{f}=0 \quad (7)$$

where $c_{11}=\lambda+2\mu=\alpha^2\rho$ and $c_{44}=\mu=\beta^2\rho$ are the isotropic-elastic stiffness modulii.

The wave equation as its written in equation (7) can be re-parameterized in terms of any three elastic modulii. Because the FWI gradient consists of terms of the form $\partial\mathbf{S}/\partial\mathbf{m}$ which are derivatives of the wave equation operator with respect to the model, the parameters that are chosen for the expression of equation (7) also effect the gradient, and therefore the model updates in FWI. Parameterizing the wave equation in terms of c_{11}, c_{44}, and ρ allows us to readily compute $\partial\mathbf{S}/\partial\mathbf{m}$ for any parameterization using the chain rule. For example, for a model parameterized in $\alpha-\beta-\rho$, with $c_{11}=\alpha^2\rho$, $c_{44}=\beta^2\rho$, the derivative of $\mathbf{S}$ with respect to α is,

$$\frac{\partial\mathbf{S}}{\partial\alpha}=\frac{\partial\mathbf{S}}{\partial c_{11}}\frac{\partial c_{11}}{\partial\alpha}+\frac{\partial\mathbf{S}}{\partial c_{44}}\frac{\partial c_{44}}{\partial\alpha}+\frac{\partial\mathbf{S}}{\partial\rho}\frac{\partial\rho}{\partial\alpha}=2\alpha\rho\frac{\partial\mathbf{S}}{\partial c_{11}}. \quad (8)$$

This section focuses on the development of a model parameterization that can incorporate prior information from well log data.

Vertical seismic profiles are an attractive acquisition geometry, due to the wealth of prior subsurface information they offer. Because a well must be drilled for the VSP sensor deployment, VSP data are often accompanied by a suite of well logs. At CaMI, this well log suite includes P-wave and S-wave sonic, and density logs, offering prior information about the P-wave velocity (V_{p}), S-wave velocity (V_{s}), and density (ρ) in the vicinity of observation well 2. Figures 4a-4c plot the well logs for V_{p}, V_{s}, and ρ respectively, and Figures 4d-Figures 4e plot crossplots of V_{s} vs V_{p} and ρ vs V_{p} respectively. Both crossplots suggest a strong relationship between V_p and V_s (Figure 4d) and V_p and ρ (Figure 4e) over the depth interval (0-350 meters) spanned by the well logs, and that there is a predictable behavior in V_s and ρ as V_p varies. This predictability can be incorporated in FWI by defining relationships between parameters, so that as one parameter (e.g. V_p) is updated, the other two parameter can be inferred from these relations.

To allow this prior information in FWI, trend lines are fit to the data using nonlinear regression. For V_p-V_s a linear relationship is often assumed, however in the near surface

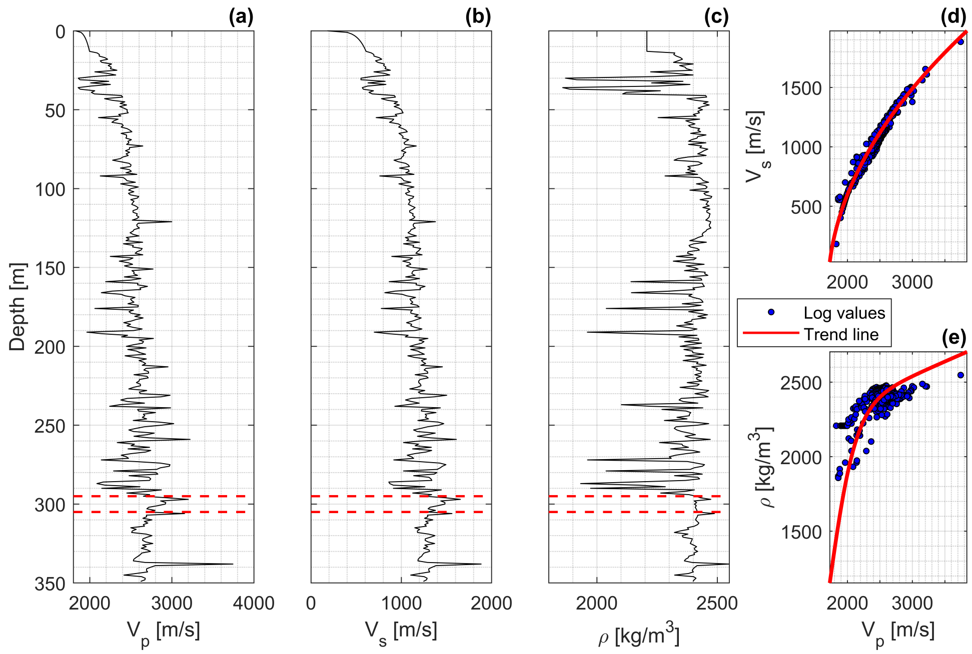

FIG. 4. Well logs from observation well 2 for (a) V_p, (b) V_s, and (c) ρ, the red dashed lines mark the reservoir boundaries. Crossplots of (d) V_s vs V_p and (e) ρ vs V_p., with the solid red lines indicating the trend lines.

this assumption is often violated. Instead I fit a quadratic function of the form,

$$V_s = \sqrt{\frac{V_p - a}{b}} + c \tag{9}$$

to the $V_p - V_s$ data where the parameters $a = 1697$, $b = 4.4 \times 10^{-4}$, and $c = -231.4$ were determined through nonlinear regression. Similarly, for $V_p - \rho$ a power-law relationship is often assumed, however for near surface structure, and certain rock types this relationship is only approximate. For better accuracy, a sigmoid of the form,

$$\rho = a + \frac{b}{1 + \exp(c * (V_p - d))} + e * (V_p - f) \tag{10}$$

is fit to the $\rho - V_p$ data where $a = -400$, $b = 2369$, $c = -4.91 \times 10^{-3}$, $d = 1715$, $e = 0.19$, and $f = -23.69$ were determined through nonlinear regression. These trend lines quantify the predicted values of V_s and ρ given a value of V_p. Figure 5 plots the log values in blue and the trend line linking all three parameters in green for values of V_p ranging from 1727 m/s to 3841 m/s which are 100 m/s below and above the minimum and maximum log values of V_p. Given a certain value of V_p, the trend line provides predicted values for V_s and ρ.

The strong correlation between V_p, V_s, and ρ motivates the idea that we can express the model in a single nonphysical parameter that encapsulates the relationship between the three parameters. The main benefits of this approach are that prior information can be intrinsically included in the inversion, preventing nonphysical combinations of V_p, V_s, and ρ and helps prevent cross-talk by only allowing updates in one parameter. For example, if

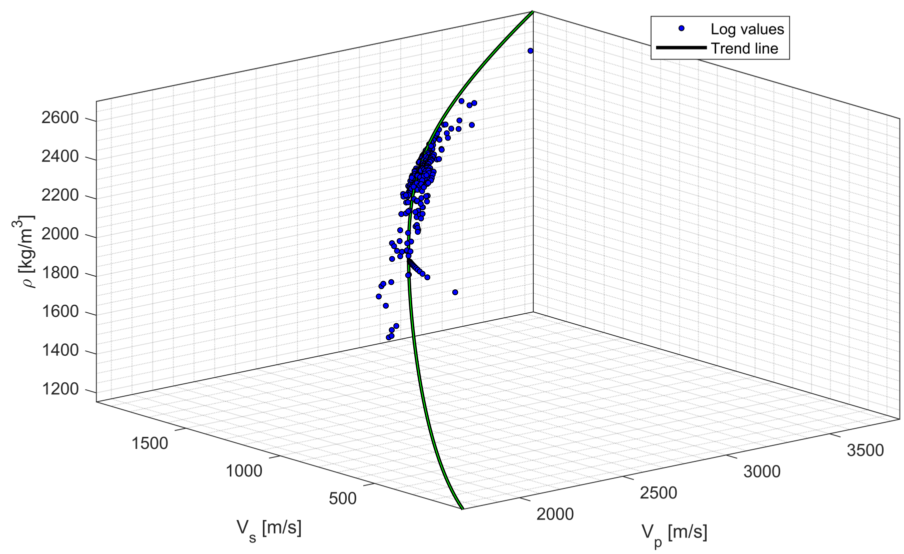

FIG. 5. Plot of the log values of V_p, V_s, and ρ (blue) and best fitting trend line (black/green).

the data encourages a certain value of V_p in the inversion, then only a single value of V_s and a single value of ρ are viable according to the trend line. One such parameterization of the trend line, which I will call η, is the arc-length along the trend line in $\alpha - \beta - \rho$ space,

$$\eta_n = \eta_{n-1} + \sqrt{(\rho_n - \rho_{n-1})^2 + (\alpha_n - \alpha_{n-1})^2 + (\beta_n - \beta_{n-1})^2}. \tag{11}$$

Using equation (11) allows for the parameterization of the model and wave equation in terms of a property that corresponds to the strong correlation in V_p and V_s and V_p and ρ. The resulting full waveform inversion sensitivities for this η parameterization are,

$$\frac{\partial \rho}{\partial \eta} = \frac{\partial \rho}{\partial \rho}\frac{\partial \rho}{\partial \eta} = \frac{\partial \rho}{\partial \eta} \tag{12a}$$

$$\frac{\partial c_{11}}{\partial \eta} = \frac{\partial c_{11}}{\partial \alpha}\frac{\partial \alpha}{\partial \eta} + \frac{\partial c_{11}}{\partial \rho}\frac{\partial \rho}{\partial \eta} = 2\alpha\rho\frac{\partial \alpha}{\partial \eta} + \alpha^2\frac{\partial \rho}{\partial \eta} \tag{12b}$$

$$\frac{\partial c_{44}}{\partial \eta} = \frac{\partial c_{44}}{\partial \beta}\frac{\partial \beta}{\partial \eta} + \frac{\partial c_{44}}{\partial \rho}\frac{\partial \rho}{\partial \eta} = 2\beta\rho\frac{\partial \beta}{\partial \eta} + \beta^2\frac{\partial \rho}{\partial \eta}. \tag{12c}$$

In equations (12a)-(12c), α,β, and ρ are values of the P-wave velocity, S-wave velocity, and density from the trend line in Figure 5. The terms $\partial\alpha/\partial\eta$, $\partial\beta/\partial\eta$, and $\partial\rho/\partial\eta$ are derivatives of these parameters with respect to η and are numerically calculated using finite difference approximations along the trend line. Using the trend line fit through nonlinear regression, and equations (11) and (12a)-(12c) provides reference values for η, V_p, V_s, ρ, $\partial\alpha/\partial\eta$, $\partial\beta/\partial\eta$, and $\partial\rho/\partial\eta$ and a means of mapping from the physical elastic parameters V_p, V_s, ρ to the nonphysical parameter η that quantifies their relation. Two models are then used, one parameterized in η for computing the FWI sensitivities and model updates, and one parameterized in V_p, V_s, and ρ for finite-difference modeling.

Mapping from well logs values of α, β, and ρ to an η model of the well logs is done in the following way. For each sample on the well log

1. Find the values of α,β, and ρ on the trend line at points n and $n+1$ that bracket the log value

$$\text{Find } \alpha_L - \alpha_T^n >= 0 \text{ and find } \alpha_L - \alpha_T^{n+1} <= 0$$

$$\text{Find } \beta_L - \beta_T^n >= 0 \text{ and find } \beta_L - \beta_T^{n+1} <= 0$$

$$\text{Find } \rho_L - \rho_T^n >= 0 \text{ and find } \rho_L - \rho_T^{n+1} <= 0$$

2. Compute the value of η corresponding to trend line values at points n and $n+1$

3. For bracketing point b linearly interpolate the corresponding η value from by computing an average of the bracketing η values weighted by the difference between the log values of α,β, and ρ and the bracketing values of each variable.

$$\eta_\alpha = \frac{\eta^n|\alpha_L^b - \alpha_T^n| + \eta^{n+1}|\alpha_L^b - \alpha_T^{n+1}|}{|\alpha_L^b - \alpha_T^n| + |\alpha_L^b - \alpha_T^{n+1}|}$$

$$\eta_\beta = \frac{\eta^n|\beta_L^b - \beta_T^n| + \eta^{n+1}|\beta_L^b - \beta_T^{n+1}|}{|\beta_L^b - \beta_T^n| + |\beta_L^b - \beta_T^{n+1}|}$$

$$\eta_\rho = \frac{\eta^n|\rho_L^b - \rho_T^n| + \eta^{n+1}|\rho_L^b - \rho_T^{n+1}|}{|\rho_L^b - \rho_T^n| + |\rho_L^b - \rho_T^{n+1}|}$$

4. Average η_α, η_β, and η_ρ to get an overall average model for η.

where y_T^n and y_T^{n+1} are values of α, β, and ρ on the the reference trend line at points n and $n+1$, y_L^B are values on the log bracketed by y_T^n and y_T^{n+1}, and η_α, η_β and η_ρ are the interpolated values of η for bracketed values of α, β, and ρ on the log.

Figures 6a-6c plot smoothed versions of the well logs in Figures 4a-4c, and Figure 6d plots the η model that corresponds to these logs, mapping with the trend line in Figure 5. The model in Figure 6d will be used as the starting model in FWI. The starting model is therefore derived from the prior information provided by the well logs, and the relationship between the isotropic-elastic parameters of interest. The wave equation and our FWI algorithm are also now parameterized in terms of η which leverages prior information, and enforces a relationship between inverted parameters. This should lead to a more a stable inversion by preventing updates that would contribute to cross-talk, and enforcing geologically meaningful model updates.

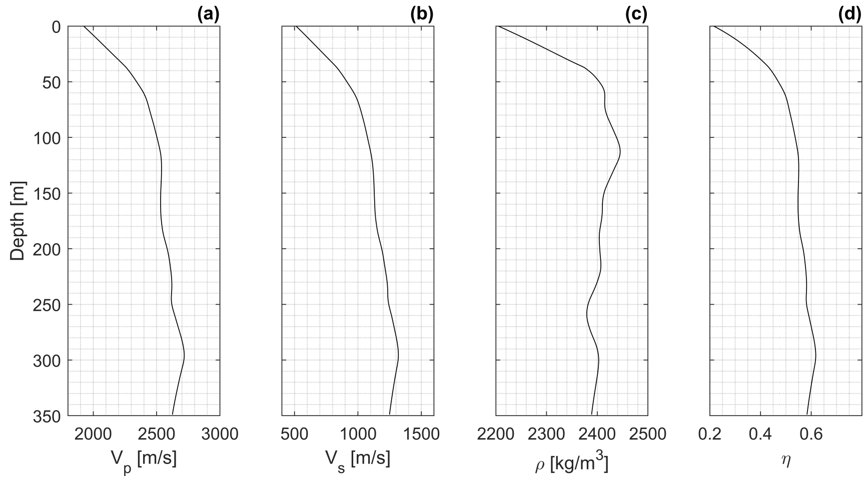

FIG. 6. Raw well logs after smoothing for (a) V_p, (b) V_s, and (c) ρ. (d) Mapped η values using the smoothed logs in (a)-(c) and the trend line in Figure 5

Effective source estimation

The near surface poses a significant challenge for land FWI applications. The unconsolidated nature of the sediment in close proximity to Earth's surface leads to very complex seismic wave propagation that is heavily influenced by surface waves, attenuation and dispersion, and mode conversions from P to S-wave motion. Additionally, prior information about these layers that could lead to better starting models and improved inversion is often missing. Well logs are rarely collected in this region (the log values in the top 20 meters of Figures 4a-4c are only approximate) and while inverse methods for near-surface velocity estimation are developing (Mills, 2017; Qu and Innanen, 2021) they remain subjects of research in application to field data. Without estimates of the near surface parameters, the complex wave propagation in the near surface cannot be accurately modeled and as a result the inversion may fail to converge as it struggles to match the near surface data.

In the absence of robust near surface information, Keating et al. (2021a) proposed a general approach for VSP data, which I modify here for application to DAS data. Instead of acquiring near surface information that allows the inversion to converge, a downward continuation method is used that inverts for the wavefield at a given depth in the subsurface that best explains the data. The idea is to strip away the near surface layers, and inject this wavefield as an effective source at depth that best explains the wavefield propagation through those near surface layers, without requiring information about the layers themselves. This effective source approach also means that prior information about the source wavelet is not required; instead it is inverted for.

What follows is a brief derivation of the source wavefield estimation procedure. A detailed discussion of this method is presented in this volume by Keating et al. (2021a). Consider the FWI objective function constrained by having to satisfy the isotropic-elastic wave equation in operator notation,

$$\min_{\mathbf{f}_{\text{eff}}} \frac{1}{2}||\mathbf{R}\mathbf{u} - \mathbf{d}||_2^2 \quad \text{subject to} \quad \mathbf{S}\mathbf{u} = \mathbf{f}_{\text{eff}}. \tag{13}$$

This is the same data fit objective function introduced in equation (1) but now minimized with respect to the source, where $\mathbf{f}_{\text{eff}}$ is the effective line source (that best explains the data) at the depth z_{eff} chosen to be at a depth below the near surface. The choice of depth requires testing, with the goal being to select the depth that allows the downgoing wavefield complexity to be explained by the effective source and mitigating the need for near surface model information.

The solution to (13) which is the gradient of the objective function with respect to the effective source $\mathbf{f}_{\text{eff}}$ is,

$$\mathbf{g} = \frac{\partial \phi}{\partial \mathbf{f}_{\text{eff}}} = \left\langle \mathbf{1}, \bar{\kappa} \right\rangle \tag{14}$$

where $\bar{\kappa}$ is the same adjoint wavefield derived in section 2.3.1 and is computed through solution to the adjoint wavefield propagation,

$$\mathbf{S}^{\dagger}\bar{\kappa} = \mathbf{R}^{\mathrm{T}}(\mathbf{Ru} - \mathbf{d}) \tag{15}$$

and $\mathbf{1}$ is a vector of ones placed at the effective source locations. The inverted effective sources are placed at the chosen depth and at every lateral grid point at that depth. This estimate of the wavefield at depth, once known, can then be treated as the effective source that then illuminates the deeper structures. The gradient in equation (14) is the cross correlation between the adjoint wavefield, which is the data residual propagated from the receiver locations, and a vector of ones at the effective source locations. This gradient updates the effective source strength using the data residuals, and finds the effective line source that best explains the field data in a least squares sense. The effective source gradient and model gradient can be simultaneously computed with minimal added cost since they both rely on the same adjoint wavefield. This allows the effective source to be refined as the model updates, and is the approach that will be taken here.

Prior information about the source geometry and source type can be used to better constrain the effective source inversion. The constraint takes the form of a regularization term that penalizes deviations in the inverted source from expectations about the source character. The constrained objective function in Lagrangian form is,

$$\mathcal{L}(\mathbf{f}_{\text{eff}}, \mathbf{u}, \kappa) = \frac{1}{2}||\mathbf{Ru} - \mathbf{d}||_2^2 + \left\langle \mathbf{S}(\mathrm{m})\mathbf{u} - \mathbf{f}_{\text{eff}}, \kappa \right\rangle + \frac{1}{4}\Upsilon||\mathrm{E} - \hat{\mathrm{E}}||_2^2 \tag{16}$$

where κ is the Lagrange multiplier on the wave equation consistency constraint, Υ is a trade-off parameter that determines the relative importance of data fit and prior source information, E is the inverted source energy and $\hat{\mathrm{E}}$ is the expected source energy that incorporates prior source information. Keating et al. (2021a) provide a detailed overview of the effective source method, practical considerations for is implementation, and a discussion of the regularization constraints required for convergence.

DAS INVERSION

Many of the regularization strategies discussed in the previous section require hyperparameters that must be fine-tuned to balance the trade-off between data fit and the reliance on prior information or expected model and source behavior. Unfortunately, this must be done through a cumbersome trial and error process. To reduce the overhead associated with this, a subset of the shots on source 1 are chosen for testing. During processing of the DAS data, a step change in the signal-to-noise ratio was observed for shots with greater than approximately 300 meters of offset. Figure 7 plots the signal-to-noise ratio (SNR) for each shot recorded on the DAS fiber, where the SNR was estimated by comparing each shots median amplitude to that of the furthest offset shot (prior to noise attenuation), which was heavily noise contaminated and assumed to provide a measurement of the noise. While the exact value of the SNR is not precise using this methodology, I am interested only in the relative SNR as a guide for selecting data for the inversion. Data from shot numbers 20-48 (marked by the vertical dashed lines on Figure 7), corresponding to shot points 1121-1171 were extracted for use in testing the inversion algorithms. Once insights about the hyperparameter tuning are understood, the full dataset will be used in the inversion.

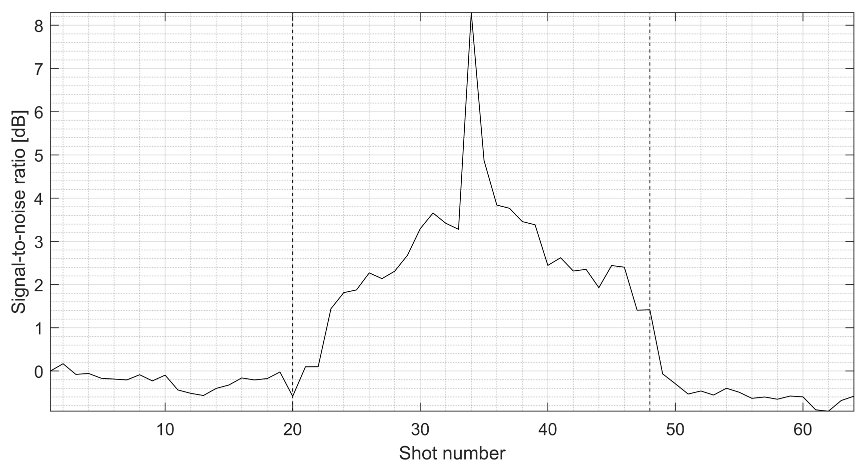

FIG. 7. Signal-to-noise ratio versus shot number for the DAS data from source line 1.

Effective source estimation

A robust initialization for the effective source is required to improve convergence of the inversion and a value for the hyperparameter Υ that determines how much emphasis is placed on data fit as opposed to expected source signature must be selected. Ideally, we want the regularization to stabilize the inversion without being overly restrictive in the effective source energy distribution. A value of Υ is chosen by first setting the effective source to be explosive at the effective source locations such that $u_x = 1$ and $u_z = 1$. The effective source is then updated using 5 iterations of unregularized ($\Upsilon = 0$) L-BFGS. At the end of those five iterations the value of the data fit objective function ($\phi_D = ||\mathbf{Ru} - \mathbf{d}||_2^2$) and the source regularization objective function $\phi_S = ||\mathrm{E} - \hat{\mathrm{E}}||_2^2$ are computed and the trade-off parameter is chosen so that $\Upsilon = (\phi_D/\phi_S)\Upsilon^*$. Many values of Υ^* were examined and it was found that a value of $\Upsilon^* = 0.1$ provided the best trade-off between data fit and effective source stability.

The effective source is then initialized by propagating wavefields through the initial model, and 15 iterations of L-BFGS are used to minimize equation (16) with $\Upsilon = 0.1(\phi_D/\phi_S)$. This process provides an estimate of the effective source that best explains the downgoing wavefields in the VSP data while maintaining a balance with the expected source signature. Figure 8a plots the theoretical energy profile for an explosive source using the field shot geometry for shot points 1121-1171. Figures 8b-8d plot the x-displacement, z-displacement, and energy profile for the inverted effective source after the 15 iterations of L-BFGS using the initial model. The expected and inverted profiles are consistent providing a good source initialization. It is important to note that the displacement profiles in Figures 8b and 8c are only constrained by needing to combine to form a reasonable energy profile. Therefore the displacement has some freedom in the inverted source profiles.

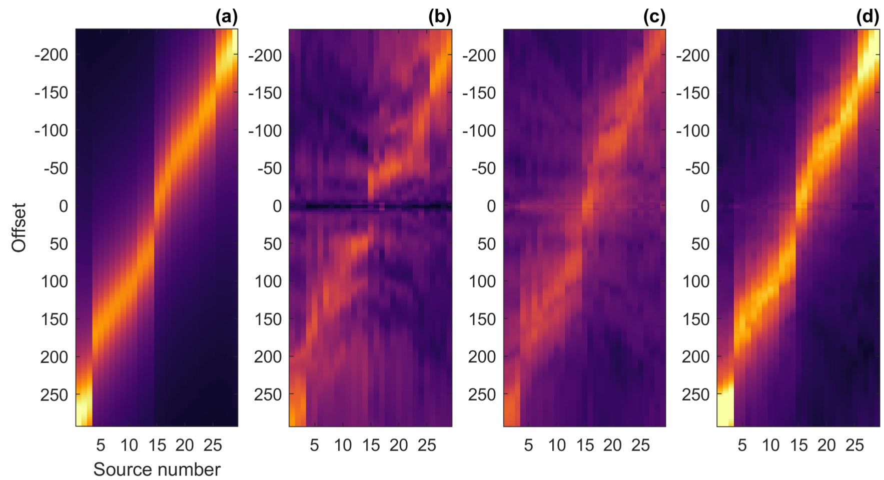

FIG. 8. (a) Theortical expected energy profile for an explosive source using the field shot geometry. Profiles of the x-displacement (b), z-displacement (c), and energy (d) for the inverted effective source.

The effective source inversion procedure presented above is only able to leverage initial model information and is therefore limited in its ability to match features in the observed data due to scattering of the elastic wavefield. Additionally, errors in the initial velocity model at long wavelength scales forces the effective source inversion to alter the phase of the source to match arrivals times in the modeled and observed data. As the model updates, the effective source is also expected to require updating to better match amplitude and phase information in the data. During the model update stage of the inversion both the effective source gradient, and the model gradient,

$$\frac{\partial \mathcal{L}(\mathbf{m}, \mathbf{u}, \lambda)}{\partial \mathbf{m}} = \left\langle \frac{\partial \mathbf{S}}{\partial \mathbf{m}} \mathbf{u}, \bar{\kappa} \right\rangle \tag{17}$$

are computed. At the end of each L-BFGS stage both the model and the source are updated which allows the effective source to be refined as the model is updated.

Model regularization

The target formation for CO_2 sequestration at the Containment and Monitoring Institutes Field Research Station is the late Cretaceous Basal Belly River Sandstone (BBRS) formation. The BBRS is a ten meter thick sandstone aquifer overlain by late Cretaceous coals (Foremost formation) and mixed shale and sandstone units. During the late Cretaceous the depositional environment for the location of present day Brooks, Alberta was a shallow inland sea, resulting in marine depositional structures. Since then, the area has been tectonically stable and beds in the area are expected to dip gently to the west (Mossop and Shetsen, 1994). This motivates the development of a regularization term that seeks to promote layering in the inverted model, and suppresses local and rapid structural variations.

The regularization term that is used for this purpose is defined as,

$$\phi_L = \Upsilon_L ||\mathbf{m} - \mathbf{Cm}|| \tag{18}$$

where Υ_L is a trade off hyperparameter that dictates the relative emphasis on data fit and layer promotion in the model **m**, and **C** is a Toeplitz matrix constructed from a Gaussian,

$$\mathrm{G} = e^{-x^2/2w_L^2} \tag{19}$$

where w_L is the desired width of the layering, and x ranges from $-2w_L$ to $2w_L$. The term **Cm** is a laterally smoothed version of the model **m** such that minimizing the objective function ϕ_L in equation (18) penalizes deviations in the updated model away from a model that has layering on the order of w_L meters wide. The gradient of equation (18) with respect to the model is,

$$\frac{\partial \phi_L}{\partial \mathbf{m}} = \Upsilon_L[2\mathbf{m} + 2\mathbf{C}^{\mathrm{T}}\mathbf{Cm} - 2(\mathbf{C}^{\mathrm{T}}\mathbf{m}^{\mathrm{T}} + \mathbf{Cm})]. \tag{20}$$

The trade-off hyper-parameter Υ_L will be determined through trial and error in the next section.

Inversion results

Using the tools developed above, which improve convergence of the field data full waveform inversion, the DAS data were inverted for the higher signal-noise-ratio data from shot points 1121-1171 representing a maximum shot-well offset of 280 meters. Modeled data will be generated using the frequency domain finite difference method (equation (7)). The inversion is computed over seven frequency bands using a multiscale approach (Bunks et al., 1995) with each frequency band consisting of eight equally spaced frequencies. The minimum frequency considered in the inversion is 10 Hz, the maximum frequency is 25 Hz, and the maximum frequency in each band is 13.5 Hz, 15.5 Hz, 17.5 Hz, 19.5 Hz, 21 Hz, 23 Hz, and 25 Hz. Each DAS shot record is converted from the time domain to the frequency domain through a temporal Fourier transform. Figure 9a plots the time domain data from shot point 1132, and Figure 9b plots the frequency domain data corresponding to this shot with receiver depth on the vertical axis and frequency on the horizontal axis. Each column of Figure 9b is the DAS data for all receivers at a single frequency.

The frequency domain data were inverted using L-BFGS with 20 iterations used to approximate the Hessian. The starting model is constructed by smoothing compressional sonic, shear sonic, and density well logs provided by Hu and Innanen (2021) and then computing the corresponding η log from equation (11). Figure 10a-10c plot the log derived P-wave velocity, log derived S-wave velocity, and density log where the black lines are the

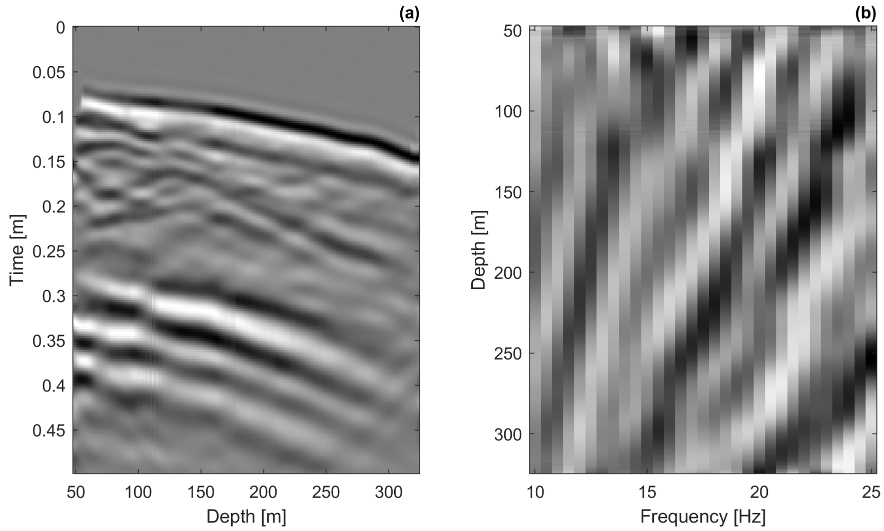

FIG. 9. (a) Time domain DAS data from shot point 1132, (b) frequency domain DAS data from shot point 1132.

log values and the red lines are smoothed log values. Figure 10d plots the corresponding η log values.

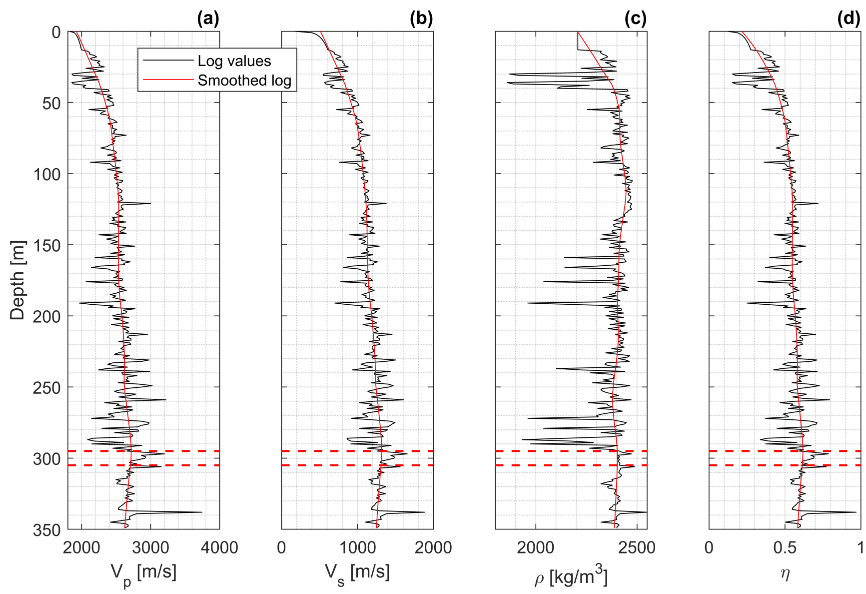

FIG. 10. (a) Sonic log derived P-wave velocity, (b) sonic log derived S-wave velocity, (c) density log, (d) corresponding log values for the special η parameterization. True log derived values are plotted in black, and the smoothed initial model is plotted in red.

Values for the layer promoting regularization width of 10, 15, 20, and 30 meters were trialed. It was determined that a 15 meter smoothing operator provided the best balance between promoting layers and allowing a reasonable amount of detail to remain in the inversion. Vales of $2 \times 10^6, 8 \times 10^6, 2 \times 10^7$, and 6×10^7 were tested for the penalty term Υ_L where the bookend values 2×10^6 and 6×10^7 were found through trial-and-error. Figure 11a plots the initial model and Figure 11b plots a smoothed version of the log derived P-wave velocity. Figures 11c-11f plot the inverted P-wave velocity models for a regularization width of 10 meters, and penalization terms Υ_L of $2\times10^6, 8\times10^6, 2\times10^7$, and 6×10^7. Figures 11g-11i plot the same for a regularization width of 15 meters. For both regularization widths a penalization term of 2×10^6 is observed to be too low and the inverted models contain many local acquisition artifacts. At the other end of the spectrum, a value of 6×10^7 appears to be too large for both a 10 meter and 15 meter smoother. While the inverted models contain few artifacts, some of the detail provided by the inversion has been lost. The inverted model in Figure 11i, with a smoother width of 15 meters and a penalization term of $\Upsilon_L = 2\times10^7$ is observed to have the best balance between retaining detail and limiting the inclusion of acquisition and structural artifacts. Encouragingly, the inverted layers appear to dip to the west (especially at approximately 175 meters depth) as expected for this area.

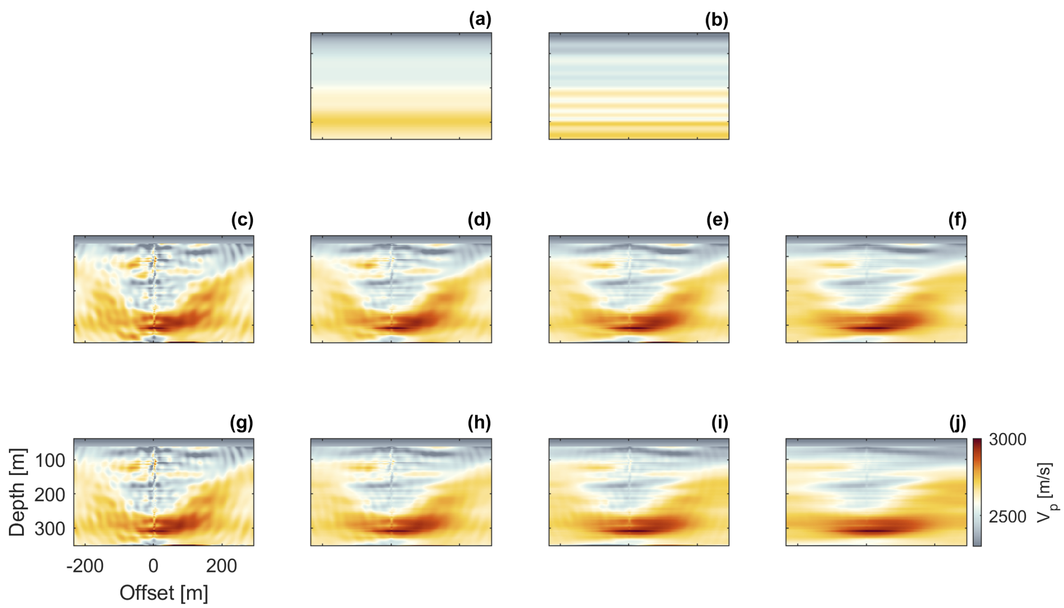

FIG. 11. (a) Initial model, and (b) P-wave velocity log smoothed to seismic resolution. Inverted P-wave velocity models using DAS data for (c) $w_L = 10$m, $\Upsilon = 2\times10^6$, (d) $w_L = 10$m, $\Upsilon_L = 8\times10^6$, (e) $w_L = 10$m, $\Upsilon_L = 2\times10^7$, (f) $w_L = 10$m, $\Upsilon_L = 6\times10^7$, (g) $w_L = 15$m, $\Upsilon = 2\times10^6$, (h) $w_L = 15$m, $\Upsilon_L = 8\times10^6$, (i) $w_L = 15$m, $\Upsilon_L = 2\times10^7$, and (j) $w_L = 15$m, $\Upsilon_L = 6\times10^7$.

Elastic full waveform inversion has conventionally assumed access to orthogonal measurements of particle velocity (when considering geophone measurements) or particle acceleration (when data are supplied by accelerometers as in this study). The single component nature of DAS recording is expected to result in less robust parameter estimates due to an insensitivity to wavefields causing strain perpendicular to the fiber axis (mostly S_V motion at near-offset). Figures 12a-12c plot the time domain shot records from shot point 1137 for the vertical and H_{max} component of the accelerometer data, and the DAS data respectively. Figures 12d-12f plot the same for the frequency domain shot records. Comparison of the accelerometer data and DAS data shows that the DAS data correlates strongly with the vertical component of the accelerometer data, but lacks detail about the converted shear wave reflections present in the H_{max} accelerometer data. This result is expected since a straight DAS fiber in a vertical well is proportional to $\partial u_z/\partial z$. I am interested in how this reduced sensitivity affects parameter estimates provided by FWI.

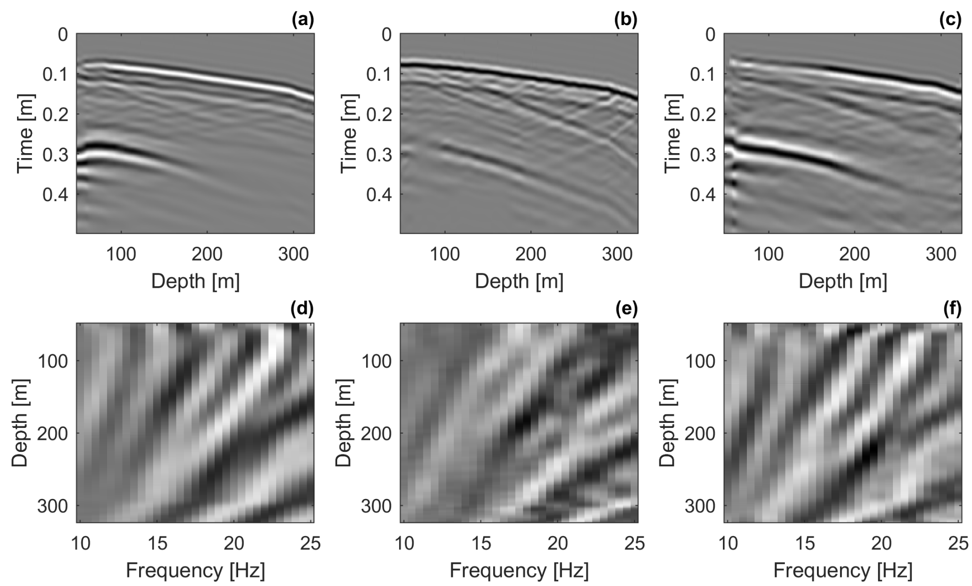

FIG. 12. Time domain shot records from shot point 1137 for (a) vertical component of the accelerometer data, (b) maximum horizontal component of the accelerometer data, (c) DAS data. Frequency domain data from shot point 1137 for (d) vertical component of the accelerometer data, (e) maximum horizontal component of the accelerometer data, (f) DAS data

To examine this, the same FWI algorithm and optimization schedule is used to invert the accelerometer data over the same range of shot points as the DAS data. The accelerometer data consists of 9 additional shots that were not recorded on the DAS survey due to a failure of the interrogator hardware. The same process was used to investigate the optimal regularization parameters for the accelerometer data and it was observed that $w_L = 15$ meters, and $\Upsilon_L = 6 \times 10^7$ provided the best trade off for the accelerometer inversion. Figures 13a-13c plot the parameter estimates for P-wave velocity, S-wave velocity, and density using the accelerometer data, and Figures 13d-13f plot the same results from inverting the DAS data with $w_L = 15$ meters, and $\Upsilon = 2 \times 10^7$. Figures 14a-14c plot the inversion results for P-wave velocity, S-wave velocity, and density through a profile at 20 m offset. The black dashed lines are the initial model, the solid black lines are a smoothed version of the well log, the blue lines are the DAS inverted models, and the red lines are the accelerometer inverted models. Overall the inverted models from the accelerometer data and those from the DAS data contain similar structure, but also have different features. Observation of the plots in Figures 14a-14c suggest that the models from the DAS inversion are a better match to the smoothed well log in the shallow intervals, but that the inverted models from the accelerometer data correlate more strongly to the log data in the deeper intervals. This suggests that the inversion may benefit from inclusion of both datasets.

Figure 15a plots the field data from shot point 1139, Figure 15b plots the DAS data modeled from the inverted models of Figures 13d-13f, and Figure 15c plots the field data (black), data modeled in the initial model (blue), and the data modeled in the inverted model (red) for 25 Hz. Figure 15d plots the objective function $||\mathbf{Ru} - \mathbf{d}||_2^2$ relative to the objective

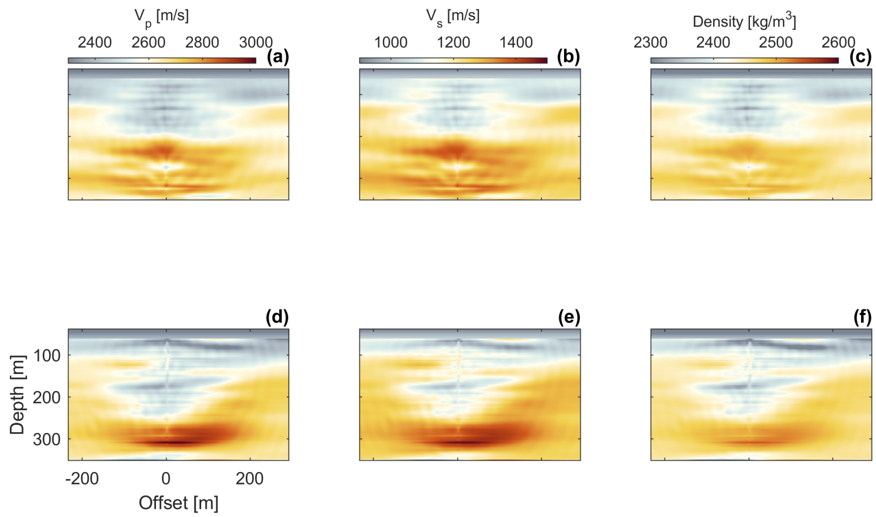

FIG. 13. Inversion results from the accelerometer data for (a) P-wave velocity, (b) S-wave velocity, and (c) density. (d)-(f) The same results acquired using the DAS data.

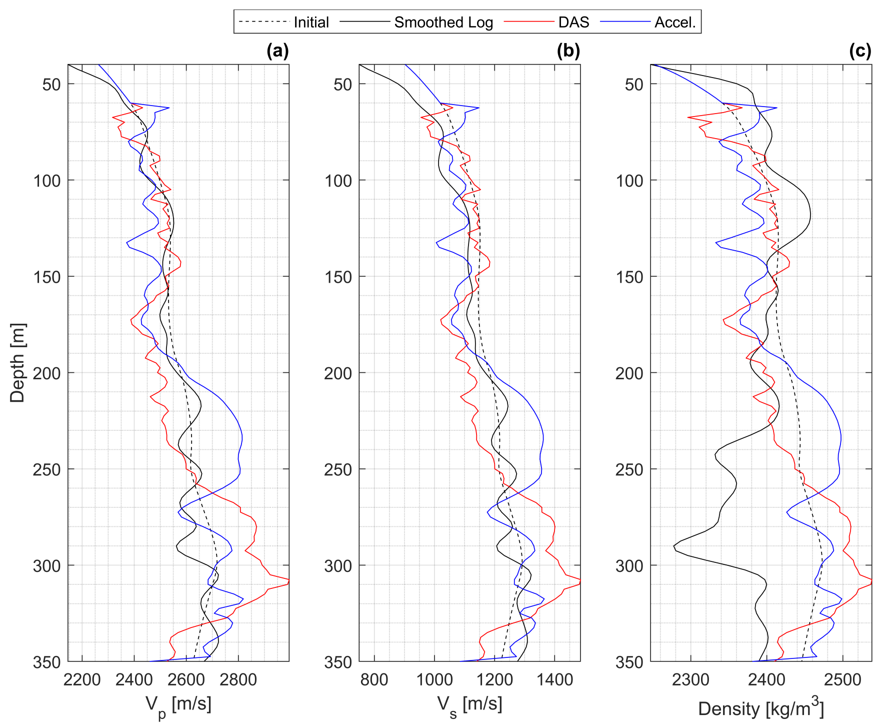

FIG. 14. Inversion results at an offset of 20 mters for (a) P-wave velocity, (b) S-wave velocity, and (c) density. The black dashed lines are the initial model, the solid black lines are a smoothed version of the well log, the blue lines are the DAS inverted models, and the red lines are the accelerometer inverted models.

function before any modeling $||\mathbf{d}|||_2^2$ which describes the data misfit after inversion relative to the initial misfit. Figures 16a-16d plot the same for the accelerometer data. These figures suggest that the FWI procedure that is employed here successfully matches the field data in generating the inverted models. The relatively low objective function values post FWI and the strong correlation between the field data and the data from the inverted models for both the accelerometer and DAS data lend confidence to the inverted models.

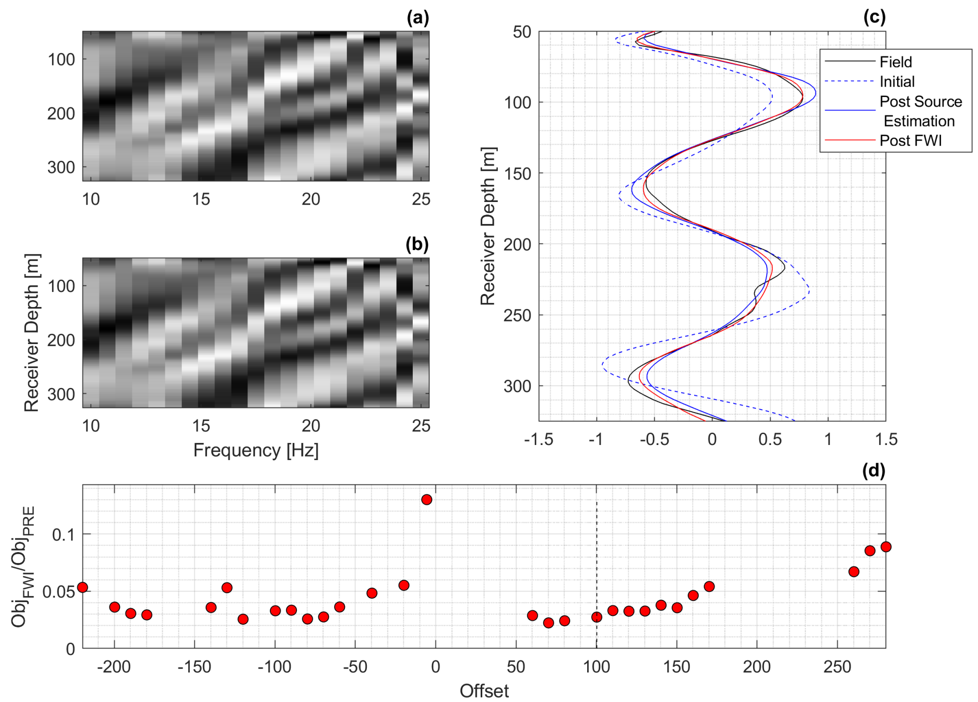

FIG. 15. (a) Frequency domain DAS field data from shot point 1139, (b) DAS data modeled using the inverted models from Figures 13d-13f. (c) Field data (black), data from initial model before (blue dashed line) and after the initial effective source estimation (solid blue line), and DAS data modeled using the inverted models (red) at 25 Hz. (d) The value of the data fit objective function relative to the initial value of the objective function versus offset. The dashed black line in (d) indicates the location of the objective function value for the data from the shot point in (a) and (b).

Simultaneous DAS and Accelerometer inversion

Insights from the inversion of DAS data and accelerometer data in isolation suggest that including both in the inversion might lead to more robust parameter updates. It is straightforward to include both accelerometer and DAS data in FWI by allowing part of the receiver matrix $\mathbf{R}$ to accommodate accelerometer data and the other portion to take on the properties of the DAS receivers. For each shot I will define $\mathbf{R}$ such that the first portion is composed of the vertical and horizontal components of the accelerometer data and the remaining portion is composed of the DAS data. The accelerometer and DAS data are normalized by their L2 norm and then balanced to each other to ensure they contribute equally in the objective function. However, it is anticipated that it might be beneficial to place greater emphasis on matching one dataset over the other. To accommodate this in FWI I define a new form of the data matching objective function,

$$\phi_D = \frac{1}{2}||\mathbf{T}(\mathbf{R}\mathbf{u} - \mathbf{d})||_2^2 \tag{21}$$

where $\mathbf{T}$ is a square diagonal trade-off matrix that balances the relative contributions of DAS and accelerometer data in FWI. Each non-zero entry in $\mathbf{T}$ has the form,

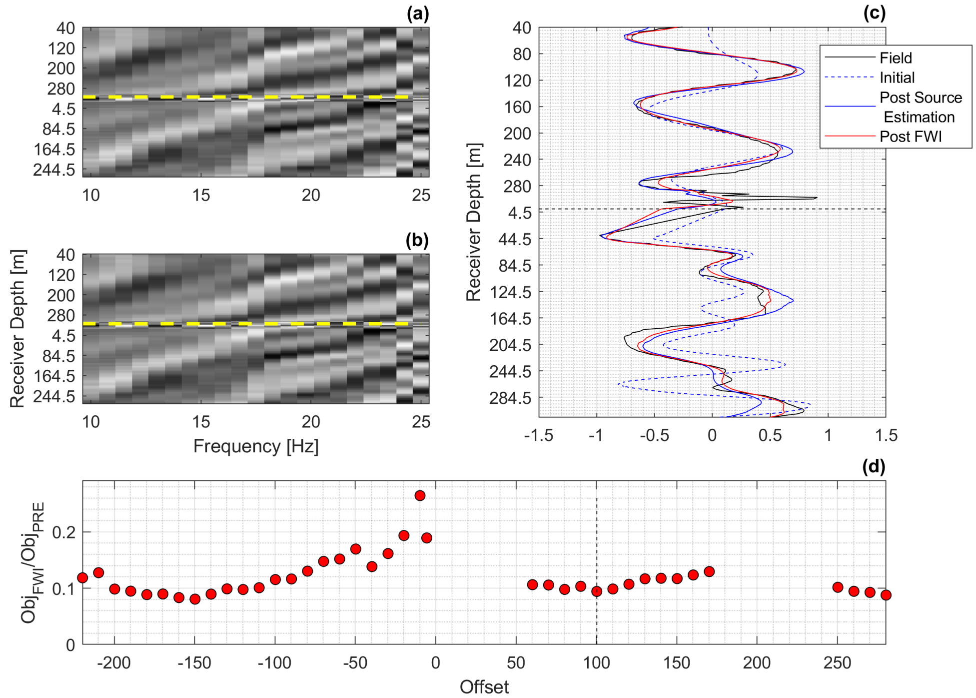

FIG. 16. (a) Frequency domain accelerometer field data from shot point 1139, (b) accelerometer data modeled using the inverted models from Figures 13a-13c. (c) Field data (black), data from initial model before (blue dashed line) and after the initial effective source estimation (solid blue line), and accelerometer data modeled using the inverted models (red) at 25 Hz. (d) The value of the data fit objective function relative to the inital value of the objective function versus offset. The dashed black line in (d) indicates the location of the objective function value for the shot point in (a) and (b) The dashed yellow lines in (a) and (b) and the dashed black line in (c) separate the vertical and horizontal components.

$$T_{ii} = \begin{cases} (1-\tau_D) & \text{for accelerometer data} \\ \tau_D & \text{for DAS data} \end{cases} \tag{22}$$

where τ_D defines the relative importance of DAS data in the inversion. A value of $\tau_D = 0$ places no emphasis on DAS data, while $\tau_D = 0.5$ balances the importance of the DAS and accelerometer data in the minimization of the objective function.

How much emphasis to place on each dataset is not apparent from the inversions results examined thus far. Instead, to test the influence of τ_D, inversions are run for $\tau_D = [0, 0.05, 0.25, 0.33, 0.5, 0.66, 0.75, 0.95, 1]$. To ensure the results are properly regularized I use a sliding scale for the layer penalty term such that $\Upsilon_L = 8\times10^7 - \tau_D(8\times10^7 - 2\times10^7)$. Figure 17a plots the smoothed P-wave velocity log, and Figures 17b-17j plot the inversion results obtained using DAS and accelerometer data in different combinations with $\tau_D = [0, 0.05, 0.25, 0.33, 0.5, 0.66, 0.75, 0.95, 1]$ respectively. Figures 17a-17i plot profiles through the inverted P-wave velocity models (blue) at an offset of 20 meters from the well and profiles of the smoothed P-wave velocity log (black) for $\tau_D = [0, 0.05, 0.25, 0.33, 0.5, 0.66, 0.75, 0.95, 1]$.

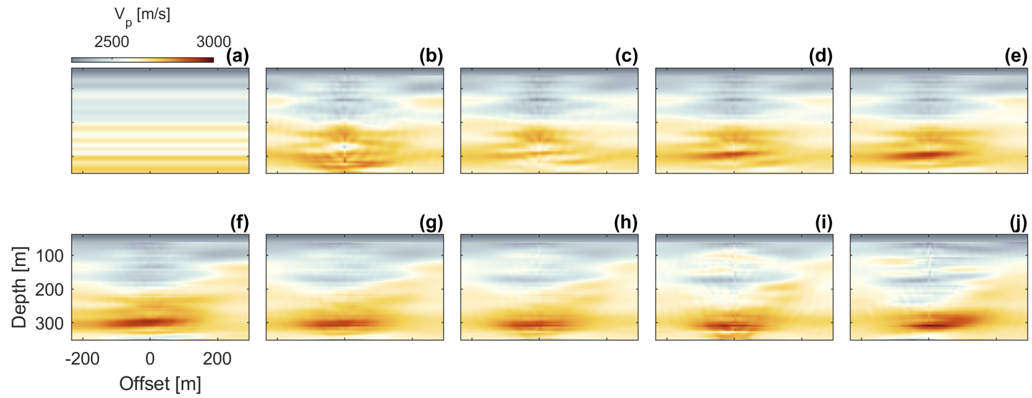

FIG. 17. (a) Smoothed P-wave velocity log. Inversion results for the objective function in equation (21) with the trade off parameter set to (b) $\tau_D = 0\%$, (c) $\tau_D = 5\%$, (d) $\tau_D = 25\%$, (e) $\tau_D = 33\%$, (f) $\tau_D = 50\%$, (g) $\tau_D = 66\%$, (h) $\tau_D = 75\%$, (i) $\tau_D = 95\%$, and (j) $\tau_D = 100\%$.

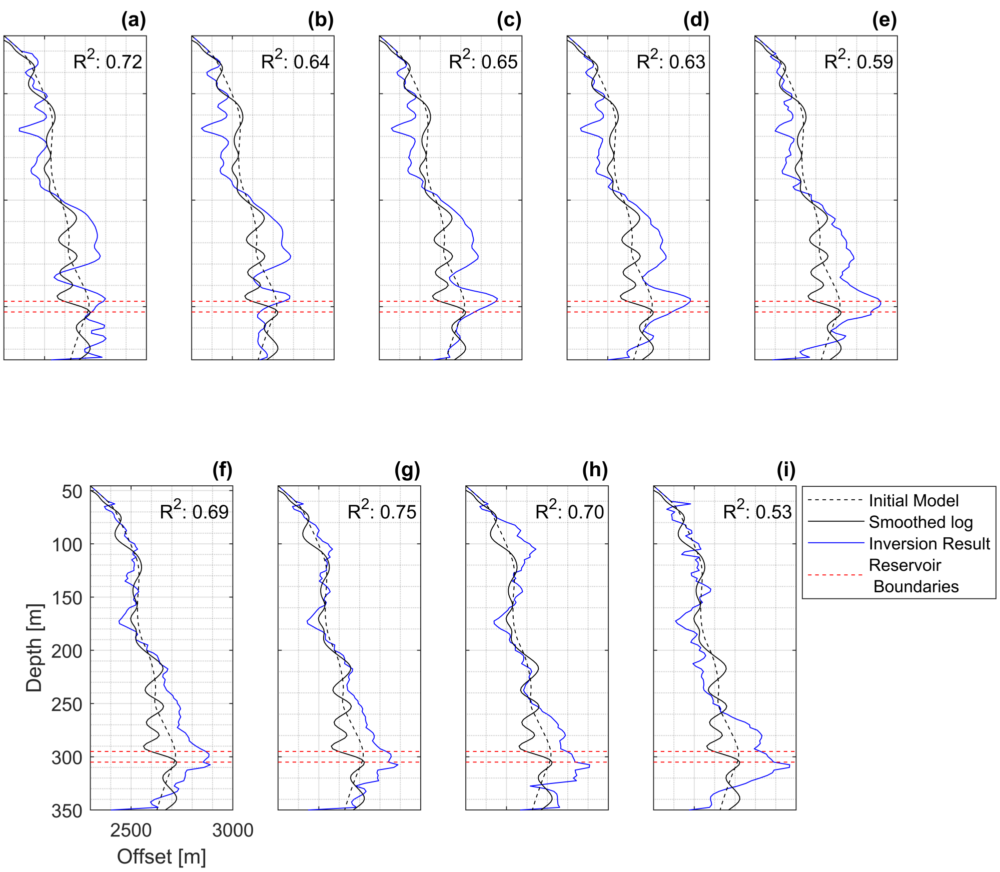

FIG. 18. Profiles through the inversion results in Figure 17 with the trade off parameter set to (a) $\tau_D = 0\%$, (b) $\tau_D = 5\%$, (c) $\tau_D = 25\%$, (d) $\tau_D = 33\%$, (e) $\tau_D = 50\%$, (f) $\tau_D = 66\%$, (g) $\tau_D = 75\%$, (h) $\tau_D = 95\%$, and (i) $\tau_D = 100\%$. The black dashed lines are the starting models, the solid black lines the smooth P-wave velocity log values, and the blue lines the inverted results an offset of 20 meters. The horizontal red lines delineate the top and bottom of the Basal Belly River Sandstone target reservoir.

Figures 17 and 18 suggest that an increasing emphasis on the DAS data has a stabilizing effect on the inverted models. While all of the inverted models tend to overestimate the velocity in the deeper subsurface sections (below approximately 200 meters), the models with more emphasis on the accelerometer data tend to underestimate the velocity in the shallower section. Increasing the relative contribution of the DAS data improves the fit to the smoothed log in the shallow sections, while leading to smoother and more stable velocity updates in the deeper sections. This is observed to hold for values of $\tau_D <= 75\%$; for larger values the velocity in the shallow section becomes less stable and tends to be overestimated. In Figures 18 the correlation coefficient between the smoothed log and the inverted profiles are computed and reported in the top right corner of each subplot. The maximum correlation occurs for $\tau_D = 75\%$. Importantly, the reservoir top is marked by a sharp velocity decrease and the reservoir bottom by a sharp velocity increase which appears to be best represented by the inverted model using $\tau_D = 75\%$. Overall the inverted models recovered using $33\% \leq \tau_D \leq 75\%$ provide a consistent range of models for the subsurface P-wave velocity structure. The DAS and accelerometer data represent independent measurements, so this consistency provides some confidence to inverted models. In all of the models, the deeper velocity structure is consistently higher than the log values, suggesting that the data strongly support a velocity increase.

Encouraged by the results obtained with the partial, near-offset dataset, which includes shot points 1121-1171, I now extend this analysis to the entire dataset for source line 1 which includes shot points 1101-1197 for offsets of 480 meters east and west of the well (see Figure 2). While processing the DAS data it was observed that the DAS shots have a marked degradation of signal-to-noise ratio with offset, and that the DAS data from the far-offset shots were heavily contaminated by noise. The curvelet based de-noising, coupled with the dip rejecting FK-filter and low pass Butterworth filter was observed to remove a significant portion of this noise, but also had the possibility of adding artifacts to the data. It is therefore possible that the full data inversion will preference a stronger emphasis on the accelerometer data than was observed when considering the less noisy DAS shots. Figure 19a plots the smoothed P-wave velocity log (extended to an offset of 480 meters in each direction) and Figures 19b-19f plot the inverted P-wave velocity models for $\tau_D = 25\%, \tau_D = 33\%, \tau_D = 50\%, \tau_D = 66\%$, and $\tau_D = 75\%$. Figures 21a-21e plot the inverted models in blue for the results in Figures 19b-19f for the profile at an offset of 25 meters, marked by the black dashed lines in Figure 19. The initial models are plotted by the dashed black lines in Figures 21a-21e and the solid black lines are the smoothed P-wave log values.

Figures 20a and 20b plot the ray paths for the P-wave velocity structure and the S-wave velocity structure from six shots at long-offsets, mid-offsets, and near-offsets. The ray path coverage provides insights into which areas of the model have more complete wavefield sampling, and which portions of the model have no ray path coverage from the direct waves. This provides an estimate for the range of offsets that are expected to have meaningful model updates, and which regions of the model are expected to have negligible updates, which allows me to focus my attention to areas of interest in the model updates. Interestingly, diving waves are apparent in the ray tracing, confirming the earlier hypothesis.

Comparing Figures 18 and Figures 21 suggests that inclusion of the full dataset has sta-

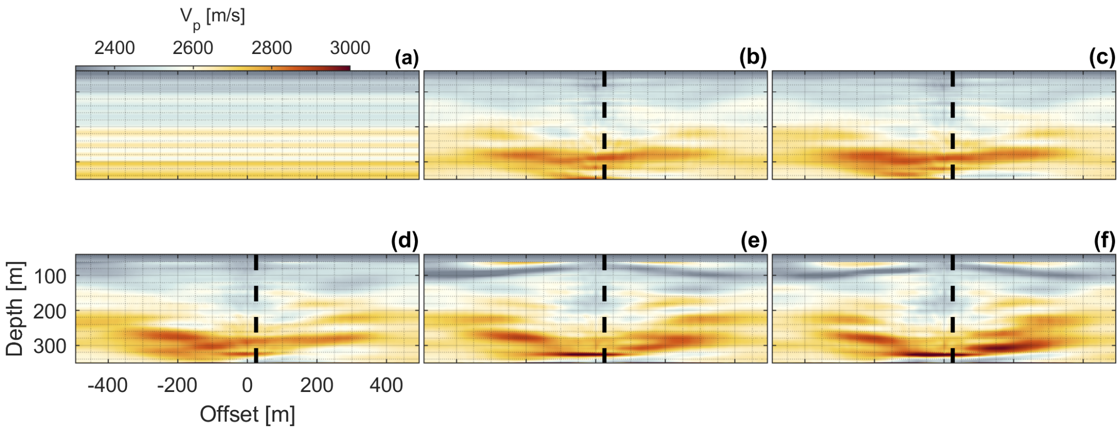

FIG. 19. (a) Smoothed P-wave velocity log. Inversion results for the objective function in equation (21) using the full dataset from source line 1 with the trade off parameter set to (b) $\tau_D = 25\%$, (c) $\tau_D = 33\%$, (d) $\tau_D = 50\%$, (e) $\tau_D = 66\%$, and (f) $\tau_D = 75\%$.

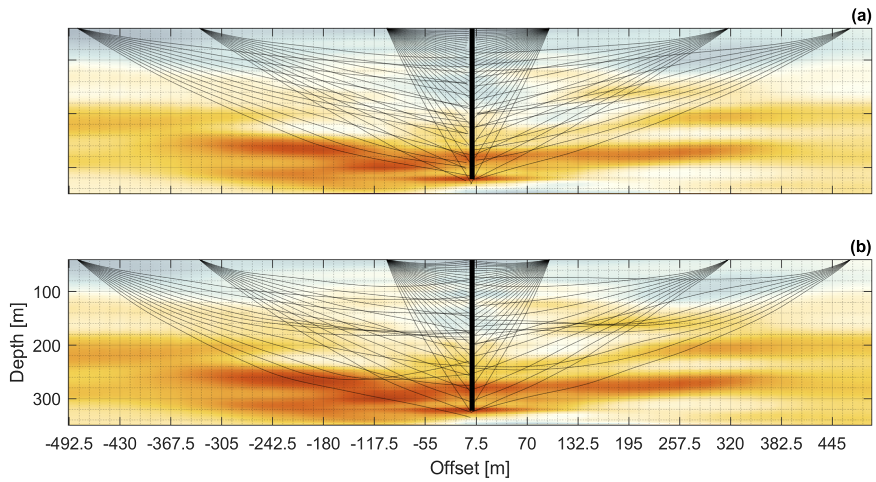

FIG. 20. (a) Ray paths through the P-wave velocity model from Figure 19d from six shot points, (b) ray paths through the S-wave velocity model using a trade off parameter of 50%. Ray paths show in black with the corresponding velocity models in the background. The solid black line marks the wellbore containing the DAS fiber and accelerometers.

bilized the inversion and leads to models that are in better agreements with the log values, and vary less rapidly. The inverted models obtained using the full dataset from source line 1 are largely comparable for all values of τ_D. Increasing the emphasis on DAS data (increasing τ_D) has increased the near surface structure as compared to those models obtained with a larger emphasis on accelerometer data. One possible explanation is that the reduced sensitivity to shear waves of the DAS fiber has resulted in a more structured near surface for the P-wave velocity to explain some of the data features. Another possibility is that the poorer DAS data quality at far offset and the processing has lead to artifacts, and that as FWI tries to match these artifacts it results in erroneous updates. Regardless, too much emphasis on the DAS data appears to result in erroneous near surface velocity updates due to poor far-offset data quality.

Figure 22 plots time domain data from shot point 1132 for the DAS fiber in row 1, the vertical component of the accelerometer in row 2, and the maximum horizontal accelera-

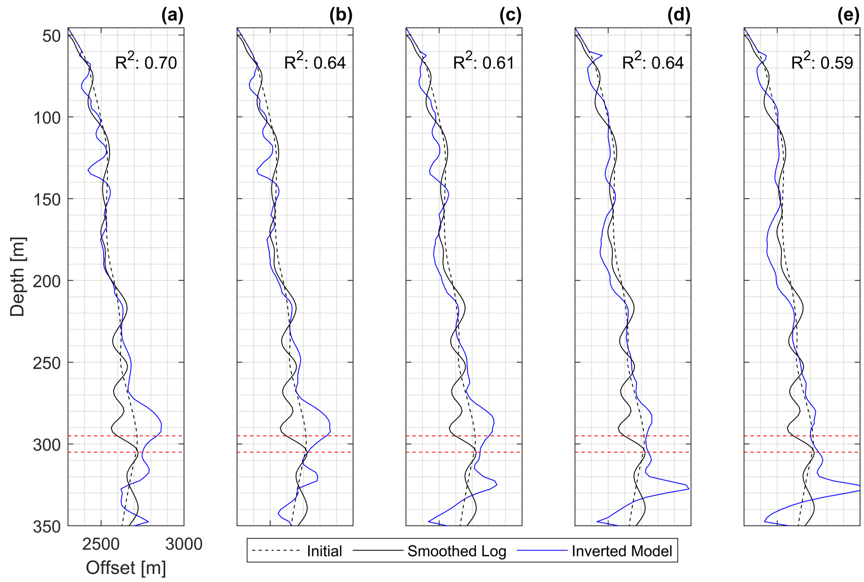

FIG. 21. Inversion results for the objective function in equation (21) using the full dataset from source line 1 with the trade off parameter set to (a) $\tau_D = 25\%$, (b) $\tau_D = 33\%$, (c) $\tau_D = 50\%$, (d) $\tau_D = 66\%$, and (e) $\tau_D = 75\%$. The dashed black line is the intital model, the solid black line the smoothed P-wave log, and the blue line is the inverted model from the dashed lines in Figure 19 at an offset of 25 meters.

tion in row 3. Figures 22a,22d, and 22g plot field-data, and Figures 22b,22e, and 22h plot modeled-data using the inverted model with equal empahsis on DAS and accelerometer data (see Figure 19d). Figures 22c,22f, and 22i plot field-data to the left and right of the yellow lines and modeled-data between the two yellow lines. For all three sensor types the modeled and field data correlate strongly, and plots Figures 22c,22f, and 22i display strong continuity between the modeled and field data. This suggests that FWI has successfully matched the field-data in forming the parameter estimates providing confidence to the results displayed in this report. Figure 22j plots the objective function values after FWI relative to their initial value showing a significant decrease in the objective function.

The model obtained with the largest emphasis on the accelerometer data ($\tau_D = 25\%$) has the largest correlation coefficient with the smoothed log value, and provides the closest match to the log, especially in the upper 225 meters. Again, a comparable class of models exists for $25\% \leq \tau_D \leq 50\%$ indicating the optimal value of τ_D falls in this range. In this case, increased emphasis on DAS data stabilizes the inversion, but too much emphasis results in model updates that contain artifacts due to the poor data quality in the far-offset shots. The results that I presented thus far are not a definitive commentary on how much emphasis should be placed on DAS data or accelerometer data in FWI. However, it has been observed that different mixtures of DAS data and accelerometer data in FWI lead to models that resolve different structures. The exact ratio that best balances the features of interest is expected to change based on the field, acquisition geometry, fiber geometry, and data quality and it is expected that an analysis similar to the one presented here will be beneficial for future monitoring surveys.

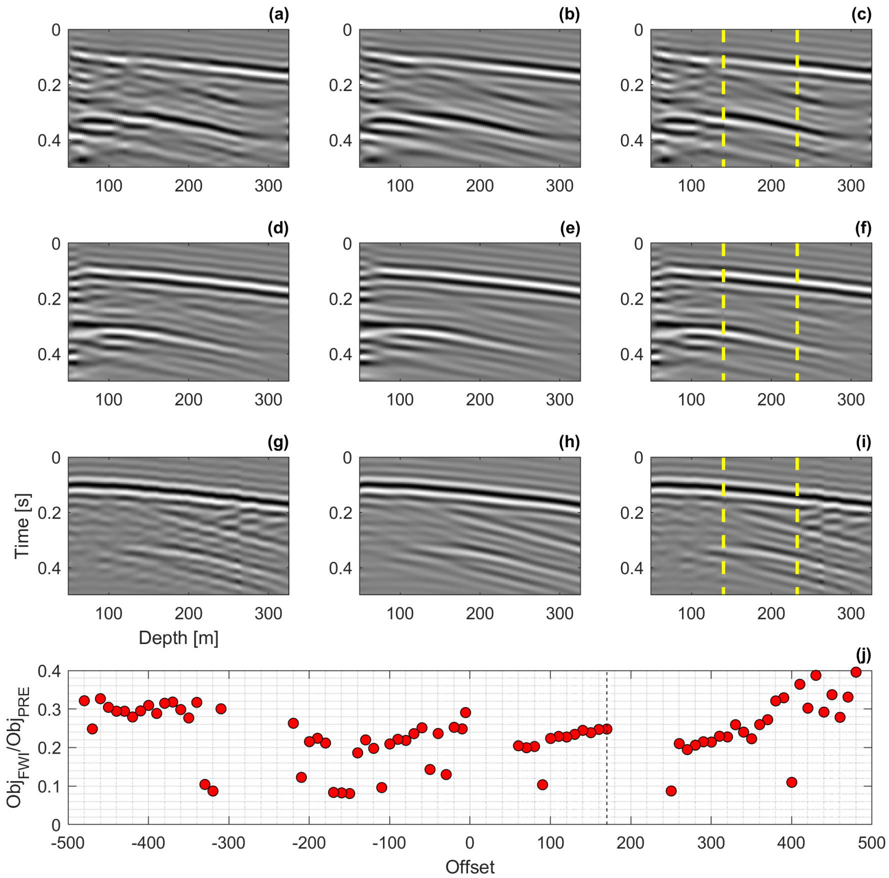

FIG. 22. Field data (a), modeled data (b), and a mixture of field and modeled data (c) for the DAS fiber. Field data (d), modeled data (e), and a mixture of field and modeled data (f) for the vertical component of acceleration. Field data (g), modeled data (h), and a mixture of field and modeled data (i) for the horizontal component of acceleration. In (c),(f), and (i) field data is plotted to the left of the first yellow line, and the right of the second yellow line, and modeled data is plotted in between the two lines. (j) The value of the data fit objective function relative to the inital value of the objective function versus offset, where the black dashed line marks the value for shot point 1132.

DISCUSSION

Multiparameter elastic FWI using seismic data acquired on land is a challenging proposition. Analysis of scattering radiation patterns for many isotropic-elastic parameterizations suggests that the successful mitigation of cross-talk requires wide source-receiver aperture (Pan et al., 2019) which is most straightforwardly provided by a mixture of surface and borehole acquisition. A mixed DAS-accelerometer acquisition offers an opportunity for cost-effective surface acquisition using a sparse accelerometer (or geophone) array coupled with a permanently installed fiber in any number of monitoring and producing or injecting wells. While an acquisition of this type was not collected during the 2018 VSP survey, and therefore not tested in this report, results from Eaid et al. (2020) suggest this would be a beneficial acquisition for alleviating some of the challenge of cross-talk associated with land FWI. Leveraging the better access to borehole geometries offered by DAS requires methods for including data from arbitrarily shaped fibers in FWI. While DAS data has been included in FWI (Podgornova et al., 2017) it is often treated through a conversion to particle velocity before being used in otherwise standard FWI. This works well for perfectly straight fiber, but is under-constrained for fiber geometries that take on the some characteristic shape. In preparation for fiber geometries that push DAS towards a multi-component sensor (Ning and Sava, 2018; Hall et al., 2021) the methods developed by Eaid et al. (2020) were applied to the data from a VSP survey acquired at the Containment and Monitoring Institutes Field Research Station. Both DAS and accelerometer inverted models, and those derived from considering varying mixtures of DAS and accelerometer data in the inversion were comparable and provided a good match to well log information. Work of the nature presented here will be crucial to fully leverage the data supplied by DAS fibers.

Land FWI faces other significant challenges, that must be addressed to help FWI converge. Near surface wavefield propagation is extraordinarily complex and incomplete wave physics coupled with poor or nonexistent prior information about the near surface can be very detrimental in land-based FWI. Additionally, although the source character is well theorized for Vibroseis type source, complexities in the forcing function can arise from changes in coupling and surface conditions from one shot to the next, leading to challenges with handling source character in FWI. Both these challenges are addressed through the development of an effective source, which is inverted for in order to explain the data. The effective source method developed by Keating et al. (2021a) mitigates the need for detailed information about the near surface, removes the need to propagate modeled wavefields through these complex layers, and accounts for changes in the source character due to surface conditions. This method proved crucial for inverting the field data, and is expected to help other applications of land based FWI where access to borehole data is available. The effective source method, its regularization, the layer based regularization, and the log-derived parameterization presented here were developed collaboratively with Dr. Scott Keating, a postdoctoral researcher with the Consortium for Research in Elastic Wave Exploration Seismology (CREWES).

Also analyzed was the inclusion of DAS and accelerometer data together in a single FWI objective function. A trade-off parameter was developed that places varying degrees of emphasis on each dataset. This is expected to be a crucial development for acquisition geometries utilizing surface geophone data, and downhole DAS data. Within the work presented here, approximately equal emphasis on DAS and accelerometer data had a stabilizing effect on the inverted models, as compared to using either dataset in isolation. Too much emphasis on the accelerometer data resulted in localized structure that is not expected for the geology of the region, and poorer match to well log data. Too much emphasis on the DAS data, which was of poorer quality than the accelerometer data at far-offset, leads to spurious near surface structure. It is expected that some combination of DAS and conventional point sensor data will benefit many land-based FWI programs, and the work presented here will help facilitate those applications.

CONCLUSIONS

DAS is poised to become a key technology for facilitating the monitoring of sequestered CO_2, and within other seismic monitoring applications. This report further develops the methods of Eaid et al. (2020) for application of elastic FWI to field data from DAS fibers in VSP geometries, and develops key methods required for successful inversion of land seismic data. The effective source was crucial for tackling the complexity of inverting land-based seismic data and reducing some of the nonlinearity in the objective function. The log-derived parameterization was key to model convergence, and appeared to explain the data as well as a full multiparameter inversion could, while converging more stably. These methods were used to aid in the inversion of field DAS data in its native strain-rate format, which is a crucial development that should transfer to the inversion of data from shaped fibers including helically wound fibers, and fibers that track horizontal and deviated wells. The strong agreement between DAS inverted models, accelerometer inverted models, and log data, and the stabilizing effects observed by using both datasets in various mixtures verifies the methods presented here.

ACKNOWLEDGMENTS

The authors would like to thank the sponsors of the CREWES project as well NSERC under the grant CRDPJ 543578-19 for making this work possible through their financial support. Matt Eaid is partially supported through a scholarship from the SEG foundation. Scott Keating was supported through the Canada First Research Excellence Fund.

The data in this report were acquired through a collaboration with Containment and Monitoring Institute (CaMI) of Carbon Management Canada (CMC). Research at the CaMI field site is supported in part by the Canada First Research Excellence Fund through the Global Research Initiative at the University of Calgary, and the CaMI.FRS Joint Industry Project.

REFERENCES

Aki, K., and Richards, P., 2002, Quantitative Seismology: University Science Books, 2 edn.

Bunks, C., Saleck, F. M., Zaleski, S., and Chavent, G., 1995, Multiscale seismic waveform inversion: Geophysics, **60**, No. 5, 1457–1473.

Cook, J., Nuccitelli, D., Green, S. A., Richardson, M., Winkler, B., Painting, R., Way, R., Jacobs, P., and Skuce, A., 2013, Quantifying the consensus on anthropogenic global warming in the scientific literature: Environmental research letters, **8**, No. 2, 24.

Eaid, M., Keating, S., and Innanen, K., 2021, Processing of the 2018 CaMI VSP survey for full waveform inversion: CREWES Research Reports, **33**, No. 6.

Eaid, M., Li, J., and Innanen, K., 2018, Modeling the response of shaped-DAS fibres to microseismic moment tensor sources: SEG Expanded Abstracts 2018, 4698–4702.

Eaid, M. V., Keating, S. D., and Innanen, K. A., 2020, Multiparameter seismic elastic full-waveform inversion with combined geophone and shaped fiber-optic cable data: Geophysics, **85**, No. 6, R537–R552.

Hall, K., Bertram, K., Bertram, M., Innanen, K., and Lawton, D., 2018, CREWES 2018 multi-azimuth walk-away VSP field experiment: CREWES Research Reports, **30**, No. 16, 1–14.

Hall, K. W., Innanen, K. A., and Lawton, D. C., 2021, Multicomponent DAS sensing: Time-series strain-rate tensor estimation from fiber data, *in* First International Meeting for Applied Geoscience & Energy, Society of Exploration Geophysicists, 442–446.

Hu, Q., and Innanen, K., 2021, Rock physics analysis for the well-log data at CaMI FRS: CREWES Research Reports, **33**, No. 22.

Innanen, K., and Eaid, M., 2017, Design of DAS fibres for elastic wave mode discrimination: CREWES Research Reports, **29**, No. 35.

Isaac, J. H., and Lawton, D. C., 2016, Brooks revisited: CREWES Research Reports, **28**, No. 33, 1–10.

Keating, S., Eaid, M., and Innanen, K., 2021a, Effective sources: removing the near surface from the VSP FWI problem: CREWES Research Reports, **33**, No. 26.

Keating, S., Eaid, M., and Innanen, K., 2021b, Full waveform inversion of VSP accelerometer data from the CAMI field site: CREWES Research Reports, **33**, No. 27.

Kuvshinov, B. N., 2015, Interaction of helically wound fibre-optic cables with plane seismic waves: Geophysical Prospecting, **64**, No. 3, 671–688.

Kweku, D. W., Bismark, O., Maxwell, A., Desmond, K. A., Danso, K. B., Oti-Mensah, E. A., Quachie, A. T., and Adormaa, B. B., 2017, Greenhouse effect: Greenhouse gases and their impact on global warming: Journal of Scientific research and reports, 1–9.

Lawton, D., Hall, K., and Gordon, A., 2018, Advances in DAS seismic monitoring for CO2 storage: SEG Technical Program Expanded Abstracts 2018, 5500–5500.

Macquet, M., Lawton, D. C., Saeedfar, A., and Osadetz, K. G., 2019, A feasibility study for detection thresholds of CO2 at shallow depths at the CaMI Field Research Station, Newell County, Alberta, Canada: Petroleum Geoscience, **25**, No. 4, 509–518.

Métivier, L., Brossier, R., Virieux, J., and Operto, S., 2013, Full waveform inversion and the truncated Newton method: SIAM Journal on Scientific Computing, **35**, No. 2, B401–B437.

Mills, A., 2017, Application of near-surface seismic characterization to sparsely sampled data sets: M.Sc. thesis, University of Calgary.

Mossop, G., and Shetsen, I., 1994, Geological atlas of the Western Canada Sedimentary Basin, `https://ags.aer.ca/reports/atlas-western-canada-sedimentary-basin`, accessed: 2021-08-30.

Ning, I., and Sava, P., 2018, Multicomponent distributed acoustic sensing: Concept and theory: Geophysics, **83**, No. 2, P1âĂŞP8.

Oreskes, N., 2004, The scientific consensus on climate change: Science, **306**, No. 5702, 1686–1686.

Pan, W., Innanen, K. A., Geng, Y., and Li, J., 2019, Interparameter trade-off quantification for isotropic-elastic full-waveform inversion with various model parameterizations: Geophysics, **84**, No. 2, R185–R206.

Podgornova, O., Leaney, S., Zeroug, S., and Liang, L., 2017, On full-waveform modeling and inversion of fiber-optic VSP data: SEG Expanded Abstracts 2017, 6039–6043.

Qu, L., and Innanen, K., 2021, Near-surface characterization using surface-wave FWI with fiberoptic data: CREWES Research Reports, **33**, No. 40.

Rodhe, H., 1990, A comparison of the contribution of various gases to the greenhouse effect: Science, **248**, No. 4960, 1217–1219.

Spackman, T. W., 2019, Novel orbital seismic sources at a CO2 storage monitoring site, Newell County, Alberta: M.Sc. thesis, University of Calgary.